International Journal of Heat and Mass Transfer 52 (2009) 3320–3333

Contents lists available at ScienceDirect

International Journal of Heat and Mass Transfer

journal homepage: www.elsevier.com/locate/ijhmt

Simulation of gas species and temperature separation in the counter-flow Ranque–Hilsch vortex tube using the large eddy simulation technique

Tanvir Farouk [a], Bakhtier Farouk [a,*], Alexander Gutsol [b]

[a] Department of Mechanical Engineering and Mechanics, Drexel University, 3141 Chestnut Street, Philadelphia, PA 19104, USA
[b] Chevron Energy Technology Company, Richmond, CA 94802, USA

ARTICLE INFO

Article history:
Received 7 August 2008
Received in revised form 10 January 2009
Accepted 10 January 2009
Available online 25 March 2009

Keywords:
Gas separation
Temperature separation
Ranque–Hilsch vortex tube
Modeling
Large eddy simulations

ABSTRACT

A computational fluid dynamic model is used to predict the species and temperature separation within a counter flow Ranque–Hilsch vortex tube. The large eddy simulation (LES) technique was employed for predicting the gas flow and temperature fields and the species mass fractions (nitrogen and helium) in the vortex tube. A vortex tube with a circumferential inlet stream of nitrogen–helium mixture and an axial (cold) outlet stream and a circumferential (hot) outlet stream was considered. The temporal evolutions of the axial, radial and azimuthal components of the velocity along with the temperature, pressure and mass density and species concentration fields within the vortex tube are simulated. Even though a large temperature separation was observed, only a very minimal gas separation occurred due to diffusion effects. Correlations between the fluctuating components of velocity, temperature and species mass fraction were calculated to understand the separation mechanism. The inner core flow was found to have large values of eddy heat flux and Reynold's stresses. Simulations were carried out for varying amounts of cold outlet mass flow rates. Performance curves (temperature separation/gas separation versus cold outlet mass fraction) were obtained for a specific vortex tube with a given inlet mass flow rate.

© 2009 Published by Elsevier Ltd.

1. Introduction

The Ranque–Hilsch vortex tube was first discovered by Ranque [1] in 1933 and was later revived and improved in efficiency by Hilsch [2] in 1947. The Ranque–Hilsch vortex tube is a simple device with no moving parts that is capable of dividing a high pressure flow into two low pressure flows of different temperatures. The vortex motion in Ranque–Hilsch vortex tube is created by tangential injection of a compressed gas. When compressed gas is injected through one or more tangential nozzle(s) into the tube, a strong vortex-like flow field is established, giving rise to a non-uniform temperature field. The gas closer to the axis is colder than the incoming feed gas, and the gas near the periphery of the tube is hotter. In the most common counter-flow vortex tube, a fraction of the feed gas exits as a cold stream through an opening in the central zone at one end near the tangential inlet, while the balance of the feed gas exits as a hot peripheral stream through a throttle valve at the opposite end which is away from the inlet. The difference in the temperature between the two gas streams is referred to as the "*temperature separation*" effect and was first observed by Ranque [1] when he was studying processes in a dust separation cyclone. Since then an intensive experimental and numerical studies of Ranque–Hilsch vortex tubes began and continues even today [3–10].

The possibility of using vortex tube as separator for gas mixture has also been investigated by several researchers [11,12]. In most of the cases it is reported that very small amount of separation takes place. Linderstrom-Lang [11] conducted detailed experimental studies to explore the possibility of using a counter-flow Ranque–Hilsch vortex tube as a gas separator. Three different gas mixtures; oxygen–nitrogen, oxygen–carbon dioxide, and oxygen–helium were used in the study. He reported very small amount of gas separation and stated that gas separation took place only due to centrifugal action. In addition his experimental findings indicated no direct relationship between temperature and gas separation. According to his experimental findings small temperature separation arise in short vortex tubes where the separation of gases is best, while the best temperature separation are obtained in long tubes where all traces of gas separation disappear. Kulkarni and Sardesai [12] conducted gas separation experiments in a vortex tube using methane–nitrogen as the inlet gas mixture. They conducted experiments for varying inlet pressure and varying hot exit pressure. However they do not report the hot exit pressure, rather expresses it as '*turns*' in the hot exit control valve. Their experimental results also indicated very small amount of gas separation. Even though, several experimental studies have been conducted by various researchers to study the possibility of gas species separation in counter-flow Ranque–Hilsch vortex tube,

* Corresponding author.
E-mail address: bfarouk@coe.drexel.edu (B. Farouk).

0017-9310/$ - see front matter © 2009 Published by Elsevier Ltd.
doi:10.1016/j.ijheatmasstransfer.2009.01.016

Nomenclature

c_p	specific heat at constant pressure (J/kg K)
C_s	Smagorinsky constant
d	diameter
D	diffusion coefficient (m^2/s)
e	specific internal energy (J/kg)
h_o	specific total enthalpy (J/kg)
k	thermal conductivity (W/m K)
$\dot{m}$	mass flow rate (kg/s)
M	molecular weight (kg/kmol)
p	pressure (Pa)
R	universal gas constant (J/mol K)
S	strain rate
t	time (s)
T	temperature (K)
$\mathbf{u}$	velocity vector (m/s)
Y	mass fraction

Greek symbols

ΔT_{hc}	temperature difference between hot and cold ends
ν_t	eddy viscosity (kg/m s)
ρ	density (kg/m^3)
τ	shear stress (N/m^2)
τ_{ij}	stress tensor component

Subscripts

c	cold gas
h	hot gas
He	helium
mix	mixture
N_2	nitrogen
r	radial direction
x	axial direction
v	vortex tube
θ	azimuthal direction
in	inlet
inner core	central region of the vortex tube
periphery	outer periphery of the vortex tube
static	static temperature
total	total/stagnation temperature

Superscripts

T	thermal

our extensive literature survey failed to provide any recent modeling studies in this area.

Despite the simplicity of the vortex tube's geometry, the energy separation phenomenon is quite intriguing. Various theories have been proposed in the literature to explain the "*temperature separation*" effect. In his pioneering work on the vortex tube, Hilsch [2] suggested that angular velocity gradients in the radial direction give rise to frictional coupling between different layers of the rotating flow resulting in the migration of energy via shear work from the inner layers to the outer layers. Other investigators have attributed the energy separation to work transfer via compression and expansion due to the flow. The different proposed mechanisms that drive the fluid motion and result in energy transfer include turbulent eddies [13], embedded secondary circulation [14] and Görtler vortices [15]. Kurosaka [16] attributed the energy separation to an acoustic streaming effect that transfers energy from the cold core to the hot outer periphery. Gutsol [17] hypothesized the energy separation to be a consequence of the centrifugal separation of micro volumes with different azimuthal velocities in the vortex tube. Despite all the proposed mechanisms, no exact theory has been able to explain the "*temperature separation*" effect convincingly.

In recent years, numerical modeling has been utilized to identify and explain the fundamental principles responsible for the energy separation in a vortex tube. Frohlingsdorf and Unger [7] used a compressible fluid dynamics model which utilized the k–ε model to include the turbulent effects. Their numerical predictions qualitatively matched the experimental results of Bruun [3]. Behera et al. [8] investigated the effect of different types and numbers of nozzles on temperature separation in a counter-flow Ranque–Hilsch vortex tube using both numerical modeling and experiments. They used compressible fluid dynamics model together with a "Renormalization Group" (RNG) k–ε model for their calculations. Aljuwayhel et al. [9] also studied the energy separation mechanism and flow phenomena in a vortex tube using both the standard k–ε model and RNG k–ε model. They report that the energy separation exhibited by the vortex tube is due to work transfer caused by a torque produced by viscous shear acting on a rotating control surface that separates the cold flow region and the hot flow region. Their predictions using the standard k–ε model was found to be in better agreement with the experimental measurements compared to that of RNG k–ε model. Similar results were also reported by Skye et al. [10]. The simulation of energy separation in a vortex tube was also reported by Eiamsa-Ard and Promvonge [18] using the standard k–ε model and an algebraic Reynolds stress model. Their computations showed that results predicted by both turbulence models generally were in good agreement with measurements but the algebraic Reynolds stress model was better. Apart from the work of Eiamsa-Ard and Promvonge [18] most of the computational studies reported in the literature used simple or first order turbulence model.

In modeling turbulence, the Reynolds averaged Navier–Stokes simulation (RANS) method attempts to model turbulence by performing time or space averaging. The averaging process wipes out most of the important characteristics of a time dependent solution. The direct numerical simulation (DNS) technique on the other

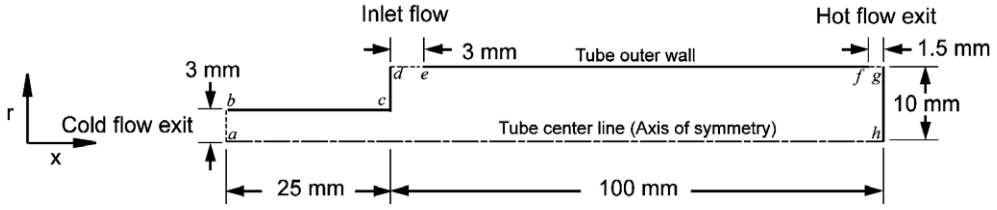

Fig. 1. Schematic of the computational domain. The origin of the coordinate system is located at point *a*.

hand attempts to solve all time and spatial scales in the velocity field. As a result, the solution is accurate but numerically very intensive. Large eddy simulation (LES) is considered somewhere in between DNS and RANS with respect to both physical resolution and computational costs. LES inherits the universality of DNS, allowing accurate prediction of the coherent structures in turbulent flows. The computational cost for LES is lower than that for DNS because the resolution requirements for LES are of the same order as those for RANS. Over the years LES technique has been successfully utilized for simulating complex turbulent flows [19–22]. Hu et al. [20] studied a methane–air diffusion flame by LES using second order moment and simplified subgrid scale combustion models, Smagorinsky–Lily and dynamic kinetic energy subgrid scale stress models. Compared to subgrid scale stress models, predictions from the dynamic kinetic energy stress models were found to be in better agreement with the experimental measurements. The effect of inner wall rotation on heat transfer in annular turbulent flow was studied using LES by Lee et al. [22]. They solved the compressible filtered Navier–Stokes equations using a second order accurate finite volume method and used a dynamic subgrid scale stress model for the subgrid scale turbulence. The simulations indicated that the modification of the turbulent structures was closely related to the increase in the Nusselt number and the wall friction coefficient. In our previous work [23] we had reported the development of a LES model using subgrid scale stress model for simulating temperature separation and flow phenomena in a counter flow Ranque–Hilsch vortex tube. The predictions indicated the LES model to be more accurate compared to the standard k–ε model.

The present work presents an axisymmetric numerical investigation of flow, temperature and gas separation (nitrogen–helium mixture) in a counter-flow Ranque–Hilsch vortex tube using a compressible Navier–Stokes model together with the LES technique. The aim of the work is to understand the mechanism responsible for temperature and gas species separation in a counter-flow Ranque–Hilsch vortex tube. The paper is organized as follows: Section 2 of the paper provides a description of the system being modeled in this study, a brief description of the model is presented in Section 3, followed by results and discussions in Section 4 and a summary with conclusions in Section 5.

2. Schematic of the problem geometry

The computational domain used for the simulations is similar to that used in our previous study [23]. Description of the computational domain was reported in [23], however we report it here for the sake of completeness and convenience. Fig. 1 depicts the computational domain. An axisymmetric flow field is considered where circumferential inlet and outlet (for the hot stream) are considered. This simplification results in considerable reduction in the computing time for the LES predictions, preserving the three-dimensional features of the flow field. Due to symmetry only half of the geometry is simulated. The line a–h is the axis of symmetry. The boundary a–b is the cold gas outlet having a radius of 3 mm. The boundary d–e is the gas flow inlet having a dimension of 3 mm. The boundary f–g located at the right most end of the vortex tube is the hot gas outlet having a width of 1.5 mm on a diameter of 20 mm. The length and the radius of the vortex tube are set to 100 mm and 10 mm, respectively. The tube length of the cold gas exit is set to 25 mm. The velocity at the inlet consists of a radial component of 20 m/s and an azimuthal component of 200 m/s. The cold exit pressure was fixed to atmospheric pressure for all the simulations. Nitrogen–helium gas mixture having 0.90 and 0.10 mass fraction of nitrogen and helium, respectively (that corresponds to 9/16 and 7/16 in molar fractions) was considered to be the working fluid. The mixture components were chosen such that one component of the mixture is sufficiently heavier than the other. The molecular weight of nitrogen is heavier by a factor of seven than that of helium. The only parameter varied during the simulations was the hot gas outlet pressure. This results in the variation of mass flows in the cold and the hot exit streams. Details of the boundary conditions considered for the simulations are discussed in the following section.

Table 2
Variable parameters for the vortex tube simulations.

Case	Hot exit pressure P_h (kPa) (absolute)	Cold mass fraction Y_c
1	191.325	0.57
2	161.325	0.28
3	171.325	0.39
4	181.325	0.48
5	201.325	0.64
6	206.325	0.69

3. Mathematical model

The compressible turbulent flows for multiple chemical species (e.g. N_2–He mixture) in the vortex tube are governed by the conservation of mass, momentum and energy equations. The equation for the conservation of mass is as follows:

$$\frac{\partial \rho}{\partial t} + \nabla \cdot (\rho \boldsymbol{u}) = 0 \tag{1}$$

where ρ is the density of the fluid mixture ($\rho = \rho_{He} + \rho_{N_2}$), $\boldsymbol{u}$ is the fluid velocity vector and ∇ is the gradient operator which has the following expression in the cylindrical co-ordinates:

$$\nabla = \hat{i}_r \frac{\partial}{\partial r} + \hat{i}_\theta \frac{1}{r} \frac{\partial}{\partial \theta} + \hat{i}_z \frac{\partial}{\partial z} \tag{2}$$

The equation for the conservation of momentum is as follows:

$$\frac{\partial (\rho u)}{\partial t} + \nabla \cdot (\rho \boldsymbol{u}\boldsymbol{u}) = -\nabla p + \nabla \cdot (\tau) \tag{3}$$

where ρ is the density of the fluid mixture, $\boldsymbol{u}$ is the fluid velocity vector, p is the static pressure and τ is the viscous stress tensor.

The energy conservation equation is as follows:

$$\frac{\partial (\rho h_o)}{\partial t} + \nabla.(\rho u h_o) = \frac{\partial p}{\partial t} + \nabla.(k_{mix} \nabla T) - \nabla.(\tau.u) \tag{4}$$

where h_o is the specific total enthalpy of the fluid mixture, T is the gas temperature, and k_{mix} is the thermal conductivity of the fluid mixture. The specific total enthalpy is expressed as follows:

Table 1
Fixed parameters for the vortex tube simulations.

Cold exit pressure P_c (kPa) (absolute)	Inlet radial velocity u_r (m s^{-1})	Inlet azimuthal velocity u_θ (m s^{-1})	Inlet pressure P_{in} (kPa) (absolute)	Inlet temperature T_{in} (K) (total)	Inlet N_2 mass fraction Y_{N_2}	Inlet He mass fraction Y_{He}	Inlet gas mixture density ρ_{in} (kg m^{-3})
101.325	−20.00	200.00	401.325	300	0.90	0.10	2.817

$$h_o = e_{mix} + \frac{p}{\rho} + \frac{1}{2}\left(u_x^2 + u_r^2 + u_\theta^2\right) \tag{5}$$

where e_{mix} is specific the internal energy of the mixture $(e_{He} + e_{N_2})$, and u_x, u_r, u_θ are the velocity components in cylindrical co-ordinates.

The total gas temperature T_{total} is expressed in the following expression:

$$T_{total} = T + \frac{1}{2c_p}\left(u_x^2 + u_r^2 + u_\theta^2\right) \tag{6}$$

where c_p is the specific heat.

For species conservation equation, we have for species '*He*':

$$\frac{\partial(\rho Y_{He})}{\partial t} + \nabla\cdot(\rho u Y_{He}) = \nabla\cdot(\rho D_{He-N_2}\nabla Y_{He}) + \nabla\cdot(\rho D^T \nabla(\ln T)) \tag{7}$$

where Y_{He} is the mass fraction of helium, D_{He-N_2} is the binary diffusion coefficient and D^T is the coefficient of thermal diffusivity. The first term on the right-hand side of Eq. (7) represents Fickian diffusion and second term represents Soret diffusion.

For a two component mixture, the remaining species (N_2) mass fraction is obtained from the following expression:

$$Y_{N_2} = 1 - Y_{He} \tag{8}$$

The density of helium and nitrogen is obtained from:

$$\rho_{He} = \rho Y_{He}, \qquad \rho_{N_2} = \rho Y_{N_2} \tag{9}$$

State equations used for the pressure is expressed in the following way:

$$p = \rho\frac{R}{M_{mix}}T \tag{10}$$

where, R is the universal gas constant, M_{mix} is the mixture molecular weight expressed as:

$$M_{mix} = \frac{1}{\frac{Y_{He}}{M_{He}} + \frac{Y_{N_2}}{M_{N_2}}} \tag{11}$$

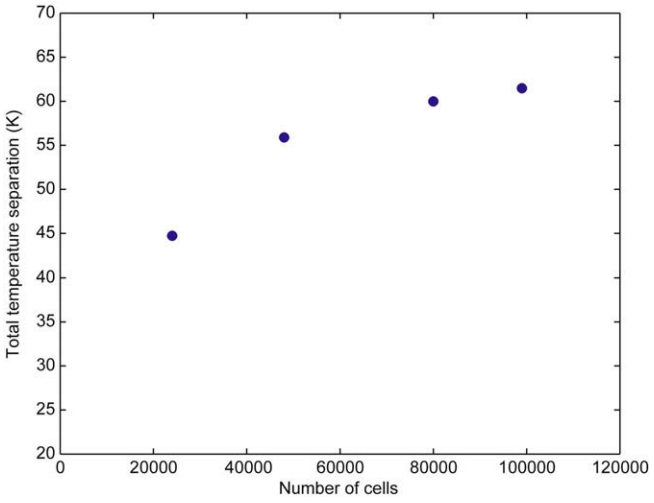

Fig. 2. Grid size dependence study on total temperature separation (case 1).

are computed from a turbulence model known as the sub-grid scale model. The sub-grid scale stress model used in the present calculation is the Smagorinsky model [24]. According to the Smagorinsky model the sub-grid scale Reynolds stress tensor is given by:

$$\tau_{ij} = \nu_t\left(\frac{\partial u_i}{\partial x_j} + \frac{\partial u_j}{\partial x_i} - \frac{2}{3}\frac{\partial u_k}{\partial x_k}\right) \tag{12}$$

where ν_t is the eddy viscosity.

The eddy viscosity is expressed in the following way:

$$\nu_t = (C_s\Delta)^2|\bar{S}| \tag{13}$$

where C_s is the Smagorinsky constant (=0.1), Δ is the filter width $(=0.06\times10^{-3})$ and S is the local strain rate which is expressed in the following way in cylindrical co-ordinates:

$$|\bar{S}| = \sqrt{2\left(\frac{\partial u_x}{\partial x}\right)^2 + 2\left(\frac{\partial u_r}{\partial r}\right)^2 + 2\left(\frac{\partial u_\theta}{r\partial\theta}\right)^2 + \left(\frac{\partial u_r}{\partial r} + \frac{\partial u_x}{\partial x}\right)^2 + \left(\frac{\partial u_\theta}{r\partial\theta} + \frac{\partial u_x}{\partial x}\right)^2 + \left(\frac{\partial u_\theta}{r\partial\theta} + \frac{\partial u_r}{\partial r}\right)^2} \tag{14}$$

3.1. Turbulence model

The LES technique is used to take into account the effect of turbulence in the vortex tube flow. The application of the LES techniques is aimed towards extracting greater temporal and spatial fidelity. In the LES technique, small scale turbulence is filtered out from the Navier–Stokes equation, and a special model is used to evaluate the small scales. The small scales

The resulting filtered Navier–Stokes equations are solved for the large scale motion which is responsible for most of the momentum and energy transport.

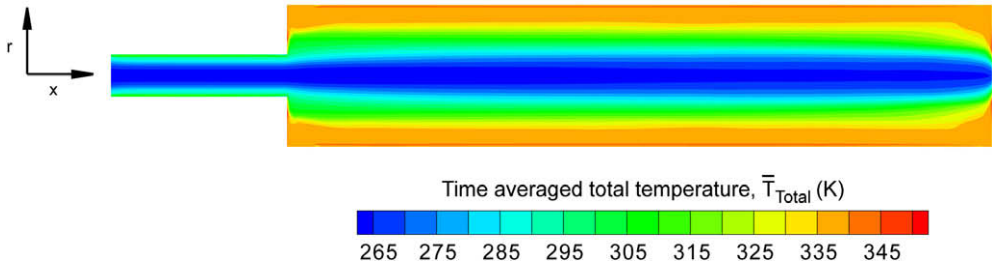

Fig. 3. Time averaged total temperature contours for the vortex tube in the *r–x* plane (case 1). Time averaging was performed between 0.4 and 0.8 s.

3.2. Boundary conditions

The boundary conditions used are similar to our previous work [23], the only difference being nitrogen–helium gas mixture at the inlet. The total mass coming into the vortex tube exits through the cold and hot exits. At the inlet a 0.90 mass fraction of nitrogen (Y_{N_2}) and 0.10 mass fraction of helium (Y_{He}) were set to be the inlet mixture. A radial velocity of $-20\ \mathrm{ms}^{-1}$ and an azimuthal velocity of $200\ \mathrm{ms}^{-1}$ was provided at the inlet. The total temperature at the inlet was set to 300 K. The pressure at the inlet was set to 401.325 kPa. Atmospheric pressure was specified at the cold exit of the vortex tube. The pressure boundary condition at the hot exit was varied in order to control the mass flow rates between the two exits. Zero gradient boundary conditions were specified for all the variables at the outflow boundaries. The tube walls were considered to be adiabatic and impermeable with no slip boundary condition for the velocity. Details of the boundary conditions are presented in Tables 1 and 2.

3.3. Numerical model

The CFD-ACE+ code [25] was used for the large eddy simulations reported in this paper. The numerical scheme for solving the governing equations is based on the finite volume approach. For the convective–diffusive terms in the mass, momentum and energy conservation equations, a second order upwind scheme [26] is used. A Crank–Nicolson scheme is used for the time derivatives in the continuity, momentum and energy equations. Time-step size of 10 μs was chosen for the Crank–Nicolson scheme. Details about the spatial grid distribution are discussed in the next section. The implicit calculations within a given time step are continued for a convergence criteria of 10^{-4} for the solving variables. The time marching calculations were terminated when a pseudo steady-state behavior was observed, which corresponds to steady fluctuations in velocity, temperature, pressure and density. In the present calculations the pseudo steady-state behavior became evident after 0.2 second (Fig. 6).

4. Results and discussion

The fixed and variable parameters for the numerical study are listed in Tables 1 and 2, respectively. Six different simulations were carried out by varying the hot exit pressure boundary values. To eliminate the errors due to coarseness of grid, analysis has been carried out for four different grid sizes 300×80 (24,000 cells), 400×120 (48,000 cells), 500×160 (80,000 cells) and 550×180 (99,000 cells) for the base case (case 1). This was done to ascertain that grid independent solutions were achieved. For the base case the hot exit pressure was set to 191.32 kPa. Following Behera et al. [8] the total temperature difference was considered to be the defining parameter for the grid-independence study. The total temperature difference is defined as the difference between the spatially and temporally averaged total temperatures at the hot and cold exits ($\Delta T_{total,hc} = \overline{T}_{total,h} - \overline{T}_{total,c}$) where, $\overline{T}_{total}$ is the time averaged total temperature defined as $\overline{T}_{total} = \frac{1}{\tau}\int_{t=t_0}^{t=t_0+\tau} T_{total}\,dt$, averaged over the exit areas. The time averaging was performed between 0.4 and 0.8 s. It can be clearly seen that increasing the number of cells beyond 80,000 (500×160 grid size) does not result in significant increase in the accuracy (Fig. 2). A grid size of 500×160 (80,000 cells) was therefore utilized for all the simulations conducted in the present work.

Fig. 3 shows the time averaged total temperature ($\overline{T}_{total} = \frac{1}{\Delta t}\int_{t=t_0}^{t=t_0+\Delta t} T_{total}\,dt$) in the r–x plane for the case 1. The separation of the total temperature fields into regions of high energy

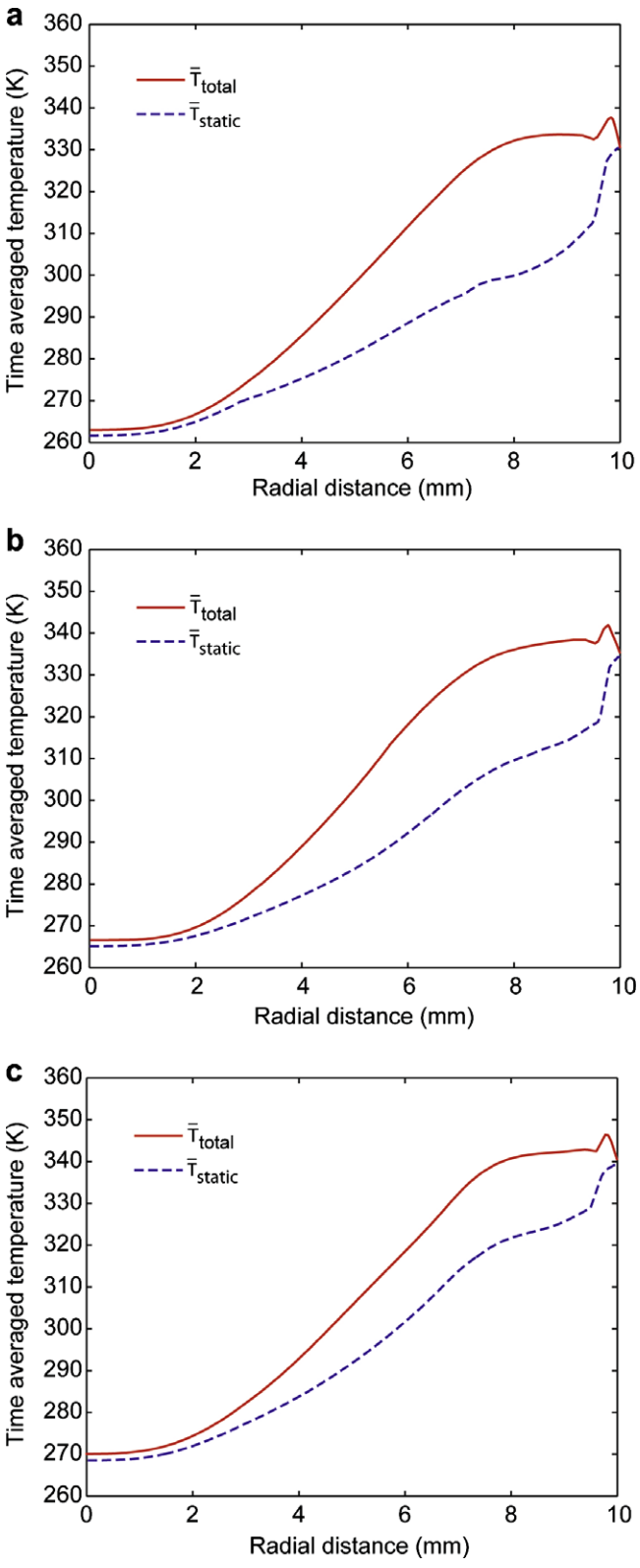

Fig. 4. Radial profiles of time averaged total temperature $\overline{T}_{total} = \frac{1}{\Delta t}\int_{t=t_0}^{t=t_0+\Delta t} T_{total}\,dt$ and static temperature $\overline{T}_{static} = \frac{1}{\Delta t}\int_{t=t_0}^{t=t_0+\Delta t} T_{static}\,dt$ at (a) x = 50 mm (b) x = 75 mm and (c) x = 100 mm (case 1). Time averaging was performed between 0.4 and 0.8 s.

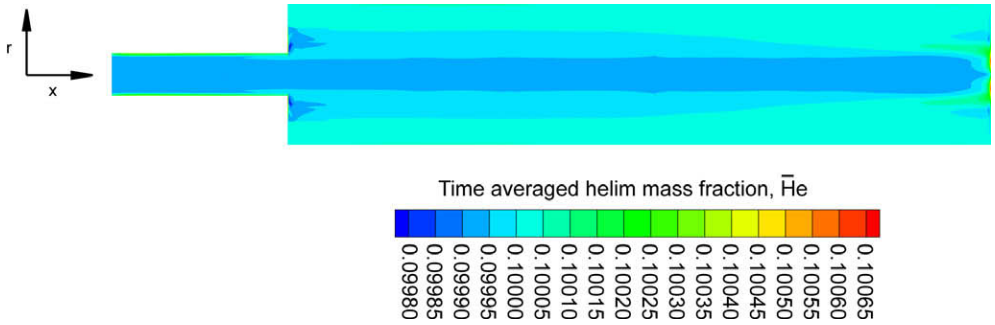

Fig. 5. Time averaged helium mass fraction contours for the vortex tube in the r–x plane (case 1). Time averaging was performed between 0.4 and 0.8 s.

(high total temperature) along the tube wall and low energy along the tube axis is evident. A distinct warm peripheral and a cold inner core flow can be seen. The predicted total temperature in the warm peripheral flow and cold inner core flow was ~335 K and ~265 K, respectively. For a hot exit pressure of 191.325 kPa a maximum hot gas total temperature of 352.5 K and a minimum cold gas temperature of 262 K were predicted where the inlet gas total temperature was 300 K. Time averaged radial profiles of the total $\overline{T}_{total}$ and static $\overline{T}_{static}$ temperature at different axial locations (x = 50 mm, x = 75 mm and x = 100 mm) for case 1 are shown in Fig. 4. At an axial distance of 50 mm, the maximum and minimum total temperatures were found to be 337 K and 263 K, respectively. The maximum total temperature was observed to exist near the periphery of the tube wall. At the tube wall the total temperature is found to decrease, this is due to the no slip boundary condition at the tube wall. The minimum total temperature region is found to span over a distance of ~2 mm, this coincides with the region of minimum azimuthal velocity (see Fig. 10). The entire cold region having a total temperature less than 300 K was found to exist up to a distance of 5.2 mm from the tube center. Similar to the total temperature, the static temperature also had the minimum near the tube axis. The minimum static temperature was found to be close to the minimum total temperature. At the tube wall the static temperature had a maximum value of 330 K. In comparison to the total temperature the static temperature was found to have a sharper gradient near the tube wall. The difference between the total and static temperature profiles is a consequence of the kinetic energy distribution in the vortex tube. Conversion of kinetic energy into the thermal one near the wall results in appearance of a sharp peak of static temperature on the wall. On the other hand, radial heat flux due to thermal conductivity increases the total temperature value near the wall. The azimuthal velocity component, which is the dominant velocity component, has two minimums equal to zero at the tube axis and at the wall, and the maximum near the tube wall (to be shown). This results in a minimum kinetic energy near the tube axis and a maximum kinetic energy near the tube wall. With an increase in the axial distance both the total and static temperatures in the cold and warm region was found to increase. At an axial location of 75 mm the total and static temperatures had a minimum temperature of 266 K and 265 K and a maximum temperature of 342 K and 334 K, respectively (Fig. 4(b)). In addition the span of the cold region was found to decrease from 5.2 mm at x = 50 mm to 4.8 mm at x = 75 mm. Similar trends were observed at an axial location of 100 mm (Fig. 4(c)). The total and static temperatures had inner core minimums of 270 K and 268 K and peripheral maximums of 345 K and 339 K, respectively. The cold region at this location spanned up to a distance of 4.5 mm from the tube center. Both the total and static temperature profiles predicted from the simulations are in very good qualitative agreement to the measurements of Eiamsa-Ard and Promvonge [18].

The time averaged helium mass fraction contours in the r–x plane of the vortex tube are presented in Fig. 5 (case 1). It was observed that very little mass separation occurred. At the periphery the helium mass fraction was 0.100032 and at the center it was 0.099915, which resulted in a separation, $\overline{Y}_{He,periphery} - \overline{Y}_{He,inner\text{-}core}$ of 1.17×10^{-4}. It is worth mentioning that simulations were also conducted without the Soret diffusion term in Eq. (7). It was found that without the Soret diffusion term the slightest gas separation (Fig. 5) ceased to occur. The absence of a distinct gas separation agrees favorably to the experimental findings of Linderstrom-Lang [11]. It is necessary to note, that another mechanism of gas separation can exist: establishing of barometric distributions for different gases in a strong centrifugal field. In that case concentration of the heavier gas should increase in the radial direction faster than that of the lighter gas. This principle is the basis of the isotope separation method in gas centrifuges [27,28]. Establishing this distribution is also a diffusion process like the Soret diffusion, therefore typical rates of these processes should be the same. Though we do not consider the equations that can describe the centrifugal separation, considering the results with including the Soret diffusion we can conclude that any diffusion processes cannot result in significant gas separation in a vortex tube.

In order to understand the temperature separation and the lack of gas species separation we systematically investigated the computed time-dependent flow, temperature and species fields in the domain. Temporal variation of the axial u_x, azimuthal u_θ and radial u_r velocity for the base case at the half radius region of the vortex tube (x = 75 mm, r = 5 mm) are shown in Fig. 6(a), (b) and (c), respectively. The period of time shown is between 0 and 0.8 s. After ~0.2 s, the system reaches a pseudo steady-state. The initial large variation diminishes but steady fluctuations are still observed. The LES scheme successfully captures the inherent velocity fluctuations in the flow field. During the pseudo steady state, the axial u_x, and radial u_r velocity was observed to fluctuate in between ±15.0 m s^{-1} and ±3.0 m s^{-1}, respectively (Fig. 6(a) and (c)). The azimuthal velocity was found to fluctuate in between 140.0 and 150.0 m s^{-1} (Fig. 6(b)). The temporal variation of temperature, pressure and density (not reported here) also showed similar pseudo steady behavior after about 0.2 s.

Fig. 7 shows the instantaneous stream lines in the r–x plane at 0.4 s for the base case. The instantaneous axial u_x and radial u_r velocity components were used to calculate the streamlines. It can be seen that there exists two regions in the vortex tube; a peripheral flow region and an inner core flow region. The peripheral flow leaves through the hot flow exit and the inner core flow leaves the vortex tube through the cold exit. A reversal of the flow in the inner core was found to be present. Vortex structures were observed throughout the tube. Small non-stationary vortices were observed to exist mostly in the inner core (cold) region of the tube. These vortices were not observed by other researchers [7–10,18], where simple and first order turbulence models were utilized.

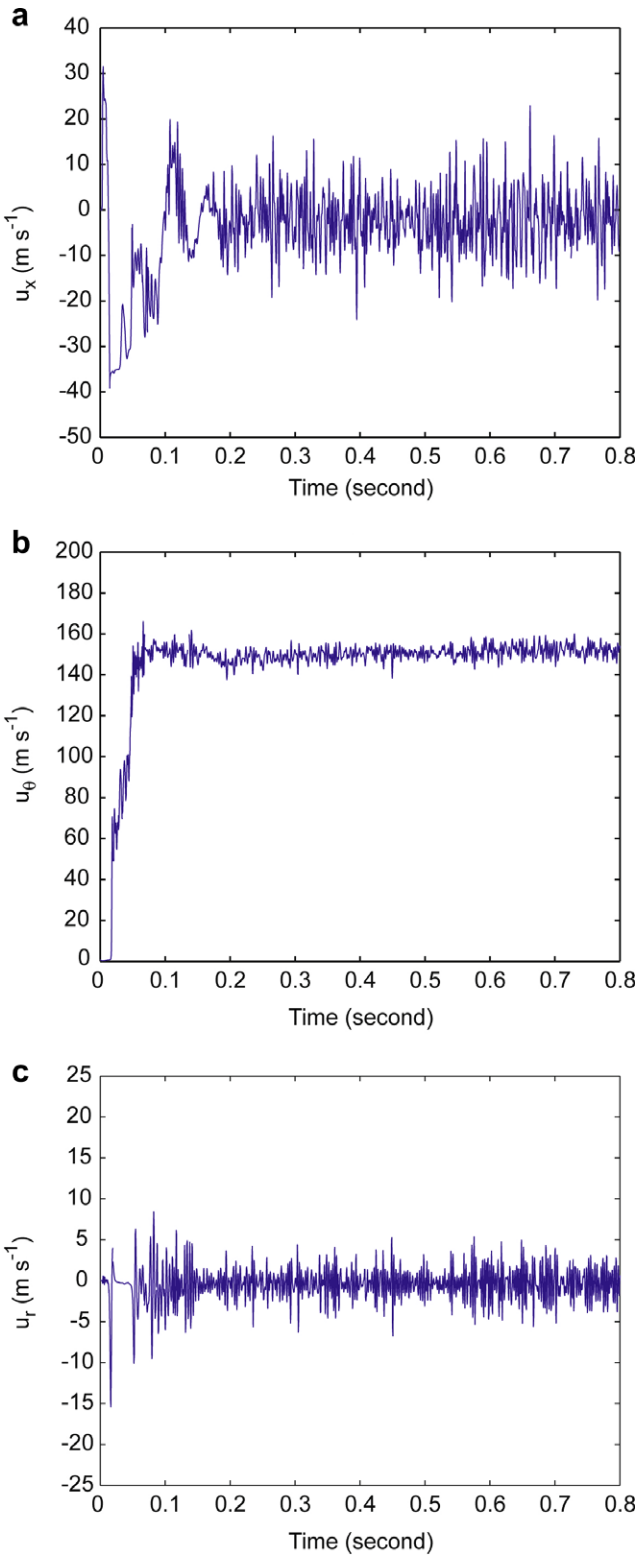

Fig. 6. Temporal variation of (a) axial velocity, u_x (b) azimuthal velocity $u\theta$ and (c) radial velocity u_r at a given location within the vortex tube (x = 75 mm, r = 5 mm) (case 1).

A small stationary vortex was also observed close to the inlet. The small vortex observed near the inlet is similar to the secondary circulation observed by Aljuwayhel [9] and Behera [8]. The presence of small vortices suggests the presence of the eddy heat flux and Reynold's stresses, which exists due to the fluctuating component of temperature and velocity. The time averaged streamlines in the r–x plane from the same case are shown in Fig. 8. The streamlines were obtained from the time averaged axial $\bar{u}_x$ and radial $\bar{u}_r$ velocity components. The time averaged streamlines clearly show two distinct regions, an outer peripheral flow and an inner core flow region. The small vortices that were present in the instantaneous streamlines ceased to exist in the time averaged streamline profiles. The vortical structures observed throughout the vortex tube at a given instant in time (Fig. 7) could be attributed as a temporal phenomena. The time averaged streamline patterns (Fig. 8) indicates that the outer peripheral flow happens to occur over a small region (~2 mm in the radial direction) whereas the inner core flow occurs in the bulk of the tube (about 8 mm in the radial direction). The peripheral flow leaving through the hot exit is seen for the fluids entering through the lower part of the inlet (near point '*e*' in Fig. 1). A small secondary circulation was seen to form near the cold end exit. The presence of the secondary circulation near the cold exit is due to the non-optimum cold exit diameter to vortex tube diameter ratio d_c/d_v of the vortex tube [8]. The d_c/d_v ratio for the present simulations is 0.30 which is lower than the optimum d_c/d_v (=0.58) value reported by Behera et al. [8]. The secondary circulation is a performance degrading mechanism in vortex tubes [8]. The secondary circulations result in enhanced mixing and increase in the cold exit temperature. By selecting an optimum cold exit diameter the formation of the secondary circulation can be prevented.

The time averaged radial profiles of the axial $\bar{u}_x$, azimuthal $\bar{u}_\theta$ and radial $\bar{u}_r$ velocity at different axial locations (x = 50 mm, x = 75 mm and x = 100 mm) are shown in Figs. 9–11, respectively (case 1). The predicted velocity profiles are similar to that observed in our previous study [23], where air was considered as the working fluid. The time averaged axial component of velocity $\bar{u}_x$ is given as, $\bar{u}_x = \frac{1}{\Delta t}\int_{t=t_0}^{t=t_0+\Delta t} u_x dt$ where t_o = 0.4 s and Δt = 0.4 s. The time averaged axial velocity profile, shows a peripheral flow with a positive value and an inner core flow with a negative value. The positive and negative values of the axial velocity denote the direction of the flow. The maximum axial velocity is found to exist near the tube wall and the direction of the flow near the wall is towards the hot end exit. The direction of the flow along the axis is towards the cold end exit and has a lesser magnitude than that at the periphery. The maximum value of the axial velocity in the periphery was found to decrease with increasing axial distance. Similar trends were observed for the axial velocity at the inner core. The axial velocity profiles show that the flow reversal takes place at ~6.5 mm from the axis of the tube for the base case (Y_c = 0.57).

Comparing the velocity components, it is observed that the azimuthal velocity has the highest value (Fig. 10). The peak value of the azimuthal velocity is larger by a factor of 2.7 than that of the axial velocity. Similar to the axial velocity the magnitude of the azimuthal velocity decreased towards the hot end exit. At axial locations of 50, 75 and 100 mm the magnitude of the azimuthal velocity was 228 m s^{-1}, 211 m s^{-1} and 198 m s^{-1}, respectively (Fig. 10). The radial profile of the time averaged azimuthal velocity indicates the formation of a small free vortex near the tube wall. The magnitude of the azimuthal velocity at the inner core was found to be negligibly small. The predicted azimuthal velocity profiles do not show the presence of a forced vortex through out the inner core flow as claimed by Behera et al. [8] and Gutsol [17]. The time averaged values of the radial velocity component $\bar{u}_r$ (Fig. 11) is significantly smaller in magnitude compared to the axial and azimuthal velocity components. Compared to the axial and azimuthal velocity the peak radial velocity was lesser by one and two orders of magnitude, respectively. The radial velocity was found to be mostly negative in the whole section (directed towards the center) with positive values near the tube wall. The time aver-

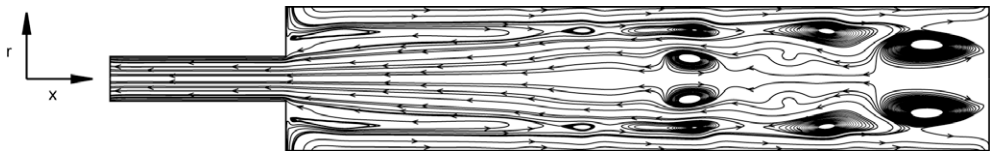

Fig. 7. Instantaneous streamlines for the vortex tube in r–x plane at 0.4 second (case 1).

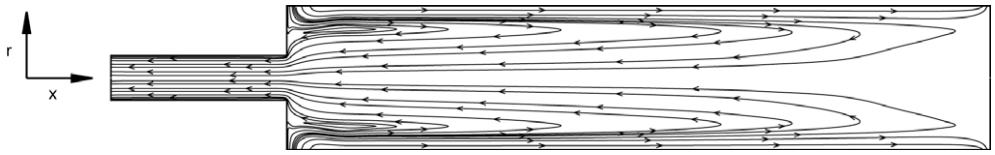

Fig. 8. Time averaged streamlines for the vortex tube in r–x plane (case 1). Time averaging was performed between 0.4 and 0.8 s.

aged radial profiles of the radial velocity at different axial locations (Fig. 11a–c) also indicates that significantly higher positive values of the radial velocity occurred near the hot periphery. Apart from the time averaged azimuthal velocity, both the axial and radial velocity profiles predictions were in good conformity with those reported by Gutsol [17].

Careful study of the data in Figs. 8–11 can explain formation of vortex structures visible in Fig. 7. First of all, Fig. 10 shows that in almost the entire volume the radial distribution of azimuthal velocity satisfies the Rayleigh stability criterion [29] $d(u_\theta\ r)/dr > 0$. Only in the cylindrical boundary layer where the azimuthal velocity decreases faster than in a free vortex, this stability criterion is violated. So, the radial distribution of azimuthal velocity cannot be a reason of formation of the vortex structures that are in the inner region of the tube. Profiles of the axial velocity u_x demonstrate very steep growth in the region 6 mm < r < 9 mm. And this shear stress is a reason of vortices in this region where the central flow changes its direction of axial motion and an average axial velocity is close to zero. Vortices in the central region, where there is no significant shear stress in any direction, are coming from the closed "hot" end of the tube (boundary g–h, Fig. 1). It is necessary to note, that in real devices the throttle valve at the hot end usually has a shape that prevents formation of such vortices that it is possible to see near the "hot end" in Fig. 7. Flat surface (boundary g–h, Fig. 1) of the "hot end" is the area where strong rotation inside the tube (that causes a strong radial pressure gradient) is terminated by the flat boundary layer. Therefore in this region there are several flows that have different directions in x–r plane: strong flow to the "hot" exit (f–g, Fig. 1) along the cylindrical surface (e–f, Fig. 1); inward-directed radial flow in the flat boundary layer caused by strong axial pressure gradient; and large (in cross-section) but slow flow of the gas that turns to the "cold" exit. Small fluctuation in this region immediately results in formation of vortices, and then the reversed "cold" flow moves these vortices which slowly dissipate their energy along the axis. Another region for the existence of strong shear stresses is the wall c–d (Fig. 1). However fluctuations in this region do not have time to form vortices because of strong radial flows that remove these fluctuations to the "cold" exit or mix them with the incoming flow.

In order to understand the temperature separation and the lack of mass separation mechanisms we also calculated the correlations between the various fluctuating components of the flow fields, temperature fields and mass fraction ($u'_x, u'_r, u'_\theta, T'_{static}$ and Y'_{He}). The $\overline{u'_x T'_{static}}, \overline{u'_r T'_{static}}$ and $\overline{u'_\theta T'_{static}}$ correlations ($\overline{u'_{i=x,r,\theta} T'_{static}} = \frac{1}{\Delta t}\int_{t=t_0}^{t=t_0+\Delta t} u'_{i=x,r,\theta} T'_{static}\, dt$ where t_o = 0.4 s and Δt = 0.4 s) are shown in Fig. 12 as contour plots in the r–x plane of the vortex tube (case 1). The eddy heat flux $\rho c_p(\overline{u_{i=x,r,\theta} T'_{static}})$ [30,31] is comprised of density, specific heat and the $\overline{u'_{i=x,r,\theta} T'_{static}}$ correlation. The $\overline{u'_{i=x,r,\theta} T'_{static}}$ correlation is the only term that takes into account the effect of the fluctuating component. The contour plots of $\overline{u'_{i=x,r,\theta} T'_{static}}$ can therefore indicate the effect of the eddy heat flux in temperature separation. It can be seen that $\overline{u'_x T'_{static}}$ have large positive values at the inner core and small negative values at the outer periphery (Fig. 12(a)). In addition $\overline{u'_x T'_{static}}$ was found to decrease with an increase in the axial distance; having the maximum near the cold exit. This is a consequence of the decreasing axial velocity with increasing axial distance (Fig. 9). The $\overline{u'_x T'_{static}}$ correlation indicates the axial component of the eddy flux to be directed from the cold end exit towards the hot end exit, which results in having a warmer inner core fluid near the hot exit (Figs. 3 and 4). Compared to $\overline{u'_x T'_{static}}, \overline{u'_r T'_{static}}$ was found to be an order of magnitude smaller (Fig. 12(b). The $\overline{u'_r T'_{static}}$ was found to have the minimum value of ~ -20 m s^{-1} K at the outer periphery of the tube, indicating an inward direction towards the center radial eddy heat flux. In this region with negative radial gradient of circulation $u_\theta\ r$, fluctuations are caused by the Rayleigh instability [29]. At the core $\overline{u'_r T'_{static}}$ had negligibly small values of ~ -0.5 m s^{-1} K. The $\overline{u'_r T'_{static}}$ contour plots indicate the transfer of the eddy heat energy in the radial direction. The values of $\overline{u'_\theta T'_{static}}$ were found to be comparable to that of $\overline{u'_x T'_{static}}$. A similar trend as that of $\overline{u'_x T'_{static}}$ was also observed with the maximum magnitude being at the inner core (Fig. 12(c)). The large positive value of $\overline{u'_\theta T'_{static}}$ at the closed end (near the hot exit) is due to the presence of high temperature there (Fig. 3). The $\overline{u'_\theta T'_{static}}$ also indicates significant eddy heat flux in the azimuthal direction.

Strong correlations observed in the axial areas in Fig. 12a and c are in agreement with the mechanism proposed in [17]. If the turbulent gas that has negative fluctuation of azimuthal velocity near the inlet migrates fast to the axis because of centrifugal separation [17] (due to the Rayleigh instability [29]), it brings to the axis region negative fluctuation of azimuthal velocity together with fluctuation of static temperature. Fluctuation of static temperature will be negative or very small if the gas comes from the inlet and arrives directly to the cold exit area. If it comes from the cylindrical boundary layer, that is warm, and arrives to the central region of the tube, the temperature fluctuation will be positive. This explains the negative correlation of $\overline{u'_\theta T'_{static}}$ in the central region. The gas also brings positive fluctuation of axial velocity as it comes from the area with higher axial velocity. This explains the positive correlation of $\overline{u'_x T'_{static}}$ at

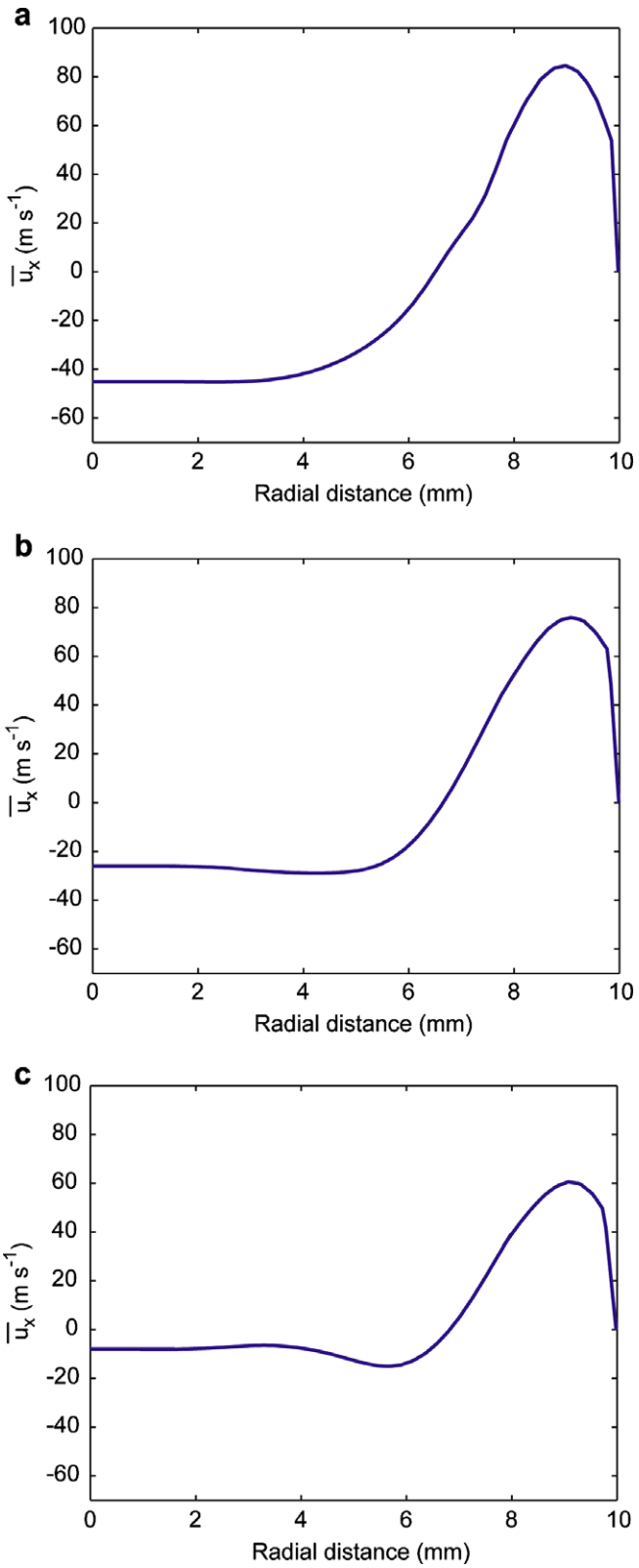

Fig. 9. Radial profiles of time averaged axial velocity $\bar{u}_x = \frac{1}{\Delta t}\int_{t=t_0}^{t=t_0+\Delta t} u_x\,dt$, at (a) $x = 50$ mm (b) $x = 75$ mm and (c) $x = 100$ mm (case 1). Time averaging was performed between 0.4 and 0.8 s.

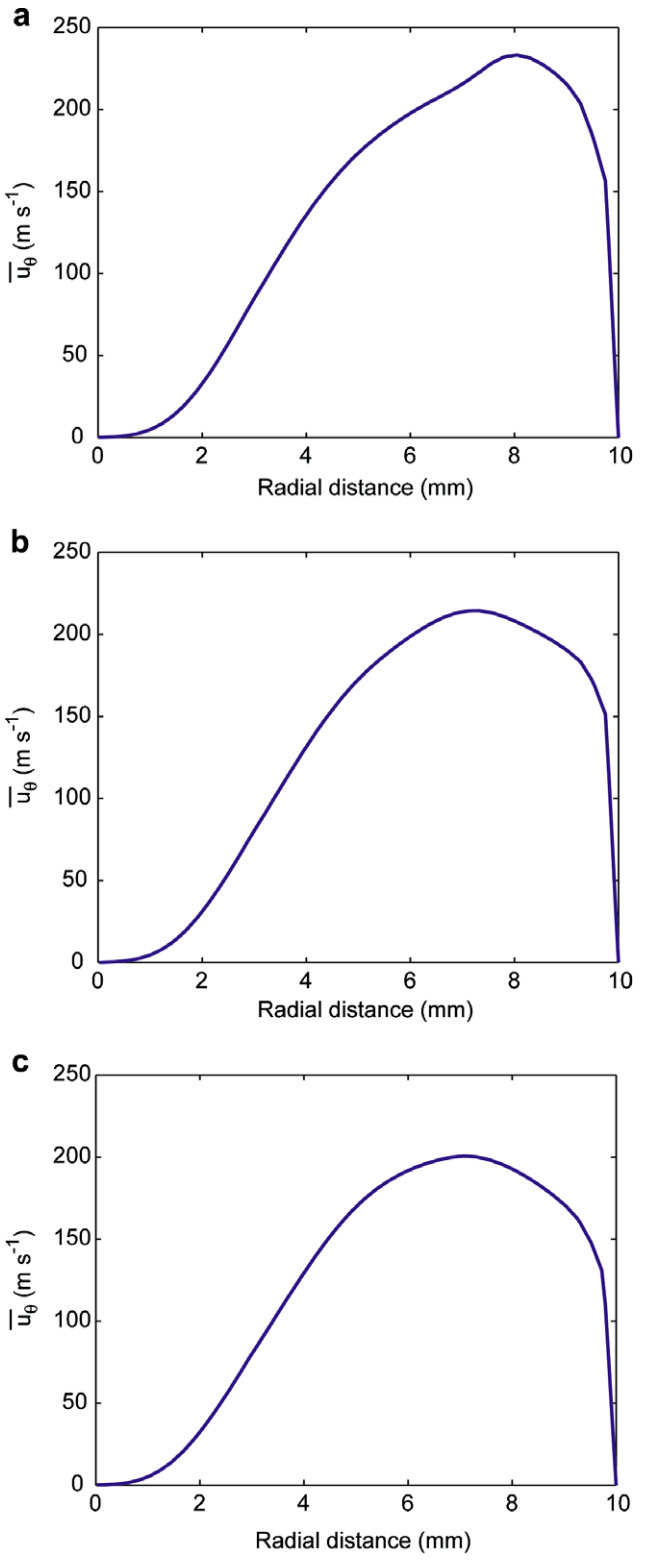

Fig. 10. Radial profiles of time averaged azimuthal velocity $\bar{u}_\theta = \frac{1}{\Delta t}\int_{t=t_0}^{t=t_0+\Delta t} u_\theta\,dt$, at (a) $x = 50$ mm (b) $x = 75$ mm and (c) $x = 100$ mm (case 1). Time averaging was performed between 0.4 and 0.8 s.

the same region. Similar effect exists at the narrow cold exit tube, where inward migration of azimuthally retarded "hot" gas accelerates the axial flow (negative correlation of $\overline{u_x' T_{static}'}$ on the axis of the cold exit tube).

Strong positive correlation $\overline{u_\theta' T_{static}'}$ near the closed end of the tube and strong irregularities in positive correlation $\overline{u_x' T_{static}'}$ near the axis at the same end, can be explained by the presence of non-stationary but well developed vortices that move in these areas (Fig. 7). The vortex formed near the closed end of the tube in Fig. 7, independent on the direction of its circulation, brings

to the almost stationary area near the axis and the end wall (see Fig. 8) the gas near the cylindrical wall which has both high azimuthal velocity and temperature. The vortices that are formed near the "hot" end and move near the axis closer to the hot exit (see Fig. 7) creates irregularities in positive correlation $\overline{u'_x T'_{static}}$: the inward flow at the boundary of these vortices splits near the axis and can increase or decrease the positive fluctuation of the axial velocity, while the temperature fluctuation is always positive. At the opposite side of the vortex all fluctuations are just opposite with the same gross result that creates irregularities in the positive $\overline{u'_x T'_{static}}$ correlation. Flow of these vortices from the "hot" end reduces the radius of the central regions with strong correlations (Fig. 12a and c) and causes formation of areas around the axis where the value of correlation $\overline{u'_x T'_{static}}$ drops and even changes the sign (see Figs. 12a and c and 13).

Fig. 13 shows the profiles of $\overline{u'_x T'_{static}}, \overline{u'_r T'_{static}}$ and $\overline{u'_\theta T'_{static}}$ along the radial distance at different axial location ($x = 50$ mm, $x = 75$ mm and $x = 100$ mm) for the base case. It can be seen that $\overline{u'_x T'_{static}}$ and $\overline{u'_\theta T'_{static}}$ are the dominant components which would result in significant eddy heat flux in the axial and azimuthal direction. In comparison $\overline{u'_r T'_{static}}$ was found to be of negligible value. Small absolute values of $\overline{u'_r T'_{static}}$ show that the flow in the vortex tube does not promote intensive turbulent heat transfer in radial direction and indeed can be used for insulation of high temperature and reactive zones as it was claimed by Kalinnikov and Gutsol [32] and Gutsol and Bakken [33]. The $\overline{u'_x T'_{static}}$ profiles indicated a large positive peak at the inner core which diminished to very small values within a distance of ~2 mm. The $\overline{u'_x T'_{static}}$ correlation was found to have small negative values at the periphery. On the other hand $\overline{u'_\theta T'_{static}}$ was predicted to have a large negative peak at the inner core. This negative peak also decreased to very small values within a distance of ~2 mm from the tube center. It is necessary to note, that because of the axial symmetry of the system, fluctuation of the azimuthal velocity at the axis are equal to zero, and this is a reason why the minimum of the correlation $\overline{u_\theta T'_{static}}$ is not on the axis. In real systems (in the case of 3-D simulation) precession of the gas rotation axis should cause significant fluctuations of azimuthal velocity and correlation $\overline{u'_\theta T'_{static}}$ should have a minimum at the system axis. Similar to $\overline{u'_x T'_{static}}, \overline{u'_\theta T'_{static}}$ was also observed to have small negative values adjacent to the tube wall. Apart from the small inner core and outer periphery region $\overline{u'_\theta T'_{static}}$ was found to have small positive values in the bulk, which spanned from ~2 mm to 8 mm. With an increase in the axial distance both $\overline{u'_x T'_{static}}$ and $\overline{u'_\theta T'_{static}}$ were found to decrease in magnitude. An exception was observed at an axial distance of 100 mm, a significant positive peak for $\overline{u'_\theta T'_{static}}$ was found (Fig. 13(c)). As explained earlier, the strong positive correlation $\overline{u'_\theta T'_{static}}$ near the closed end of the tube is a result of well developed vortices formed in this area (Fig. 7) in combination with the fact that the high temperature zone exists near the closed end (Fig. 9). In addition, the azimuthal component of velocity has large fluctuations due to the presence of the end wall. It is worth mentioning that throughout the vortex tube the large magnitudes of $\overline{u'_x T'_{static}}$ and $\overline{u'_\theta T'_{static}}$ are found to exist at the inner core which coincides with the cold temperature region (Fig. 4).

The radial profiles of $\overline{u'_x u'_r}, \overline{u'_x u'_\theta}$ and $\overline{u'_\theta u'_r}$ at different axial locations ($x = 50$ mm, $x = 75$ mm and $x = 100$ mm) for the same case is presented in Fig. 14. The Reynold's stresses $\rho \overline{u'_{i=x,r,\theta} u'_{j=x,r,\theta}}$ comprises of density and the fluctuating components of the velocity. The off diagonal components ($i \neq j$) of the Reynold's stresses are shear stresses due to eddies and have a major contribution in viscous heating [31]. The $\overline{u'_x u'_r}, \overline{u'_x u'_\theta}$ and $\overline{u'_\theta u'_r}$ correlations are therefore indicative of the shear stresses generated due to the small eddies. The radial profiles of $\overline{u'_x u'_r}, \overline{u'_x u'_\theta}$ and $\overline{u'_\theta u'_r}$ show that $\overline{u'_x u'_\theta}$ is the dominant component. Both $\overline{u'_x u'_r}$ and $\overline{u'_x u'_\theta}$ are found to be of negligibly

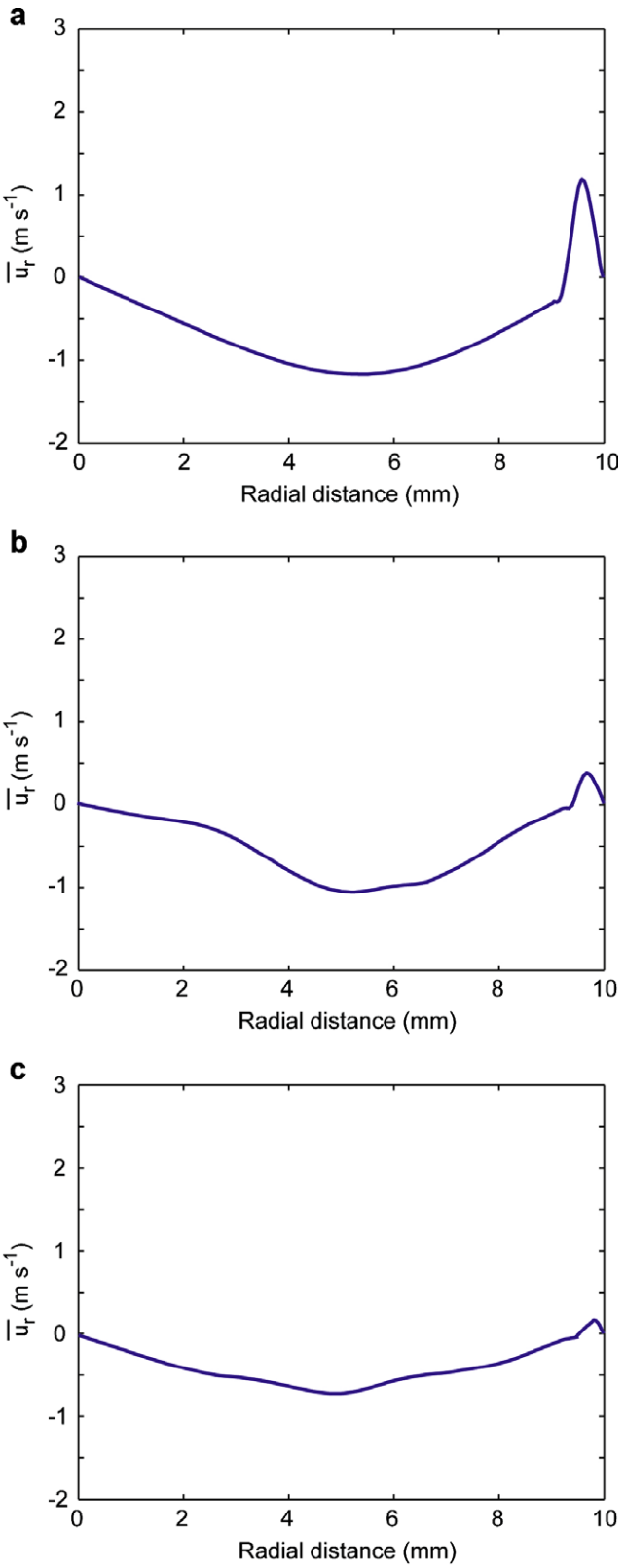

Fig. 11. Radial profiles of time averaged radial velocity $\bar{u}_r = \frac{1}{\Delta t}\int_{t=t_0}^{t=t_0+\Delta t} u_r\, dt$, at (a) $x = 50$ mm (b) $x = 75$ mm and (c) $x = 100$ mm (case 1). Time averaging was performed between 0.4 and 0.8 s.

small values. The large magnitude of $\overline{u'_x u'_\theta}$ implies the presence of large shear due to the two dominant velocity components; axial u_x and azimuthal u_θ. The magnitude of $\overline{u'_x u'_\theta}$ increases with increasing radial distance till ~1.2 mm. Beyond 1.2 mm the magnitude decreases with an eventual sign change at 2.1 mm. Apart from the small inner core region, the $\overline{u'_x u'_\theta}$ component is found to have positive values in the bulk of the tube (2.1 mm–10 mm). The peak magnitude of $\overline{u'_x u'_\theta}$ is found to be present at the inner core. Similar to the $\overline{u'_x T'_{static}}, \overline{u'_r T'_{static}}, \overline{u_\theta T'_{static}}$ (Fig. 13), the $\overline{u'_x u'_\theta}$ profiles show a decrease in the magnitude with increasing axial distance (Fig. 14a–c). The explanation for having such a distribution profile of the $\overline{u'_x u'_\theta}$ correlation is same as that for $\overline{u'_x T'_{static}}$ and $\overline{u'_\theta T'_{static}}$ correlation distributions.

The correlation between the fluctuating components of helium mass fraction and static temperature was also calculated to determine if a strong correlation similar to $\overline{u'_{i=x,r,\theta} T'_{static}}$ was present. The radial profiles of $\overline{Y'_{He} T'_{static}}$ at different axial location ($x = 50$ mm, $x = 75$ mm and $x = 100$ mm) for the base case are summarized in Fig. 15. The plots indicates that there does not exist a strong correlation between Y'_{He} and T'_{static}. Very small values of $\overline{Y'_{He} T'_{static}}$ were present at the inner core, whereas at the bulk it was almost close to zero. The weak correlation further suggests why such small amount of gas separation was observed in simulated cases due to Soret diffusion. The energy equation (Eq. (4)) has an energy flux term and also the pressure work and viscous heating as source terms. The species conservation equation (Eq. (7)), however, does not have any source term and has both Fickian and Soret diffusion as the dissipative term. The terms in the species conservation equation proposes that gas separation is only possible through diffusion. In a vortex tube the gas having sufficiently high velocity reduces the gas residence time in the tube and thereby hinders the gas separation through diffusion. The high turbulence in the vortex tube enhances the mixing rather than assisting separation.

A parametric study was carried out to investigate the effect of varying the mass flow rates at the cold and hot exits on the temperature and gas separation. This was achieved by varying the outlet pressure at the hot exit systematically (see Table 2). Following both our previous work [23] and that of Skye et al. [10], the total temperature separation at the cold and hot exits is the absolute difference between the inlet temperature and the respective exit total temperatures. The cold exit and hot exit temperature separation as a function of cold mass fraction is present in Fig. 16a and b, respectively. The time averaged total temperatures at the hot and cold ends were spatially averaged to obtain the values plotted. For the cold exit temperature separation, $|\overline{T}_{total,in} - \overline{T}_{total,coldexit}|$ (Fig. 16a) it was found that the temperature separation increased until 0.39 cold mass fraction, beyond which it decreased with an increase in the cold mass fraction. A cold mass fraction of 0.39 is the optimum mass fraction for obtaining the maximum temperature separation at the cold exit. This operating point for the system (maximum cooling) depends both on the geometric parameters and the inlet conditions of the incoming flow. The maximum cold temperature sep-

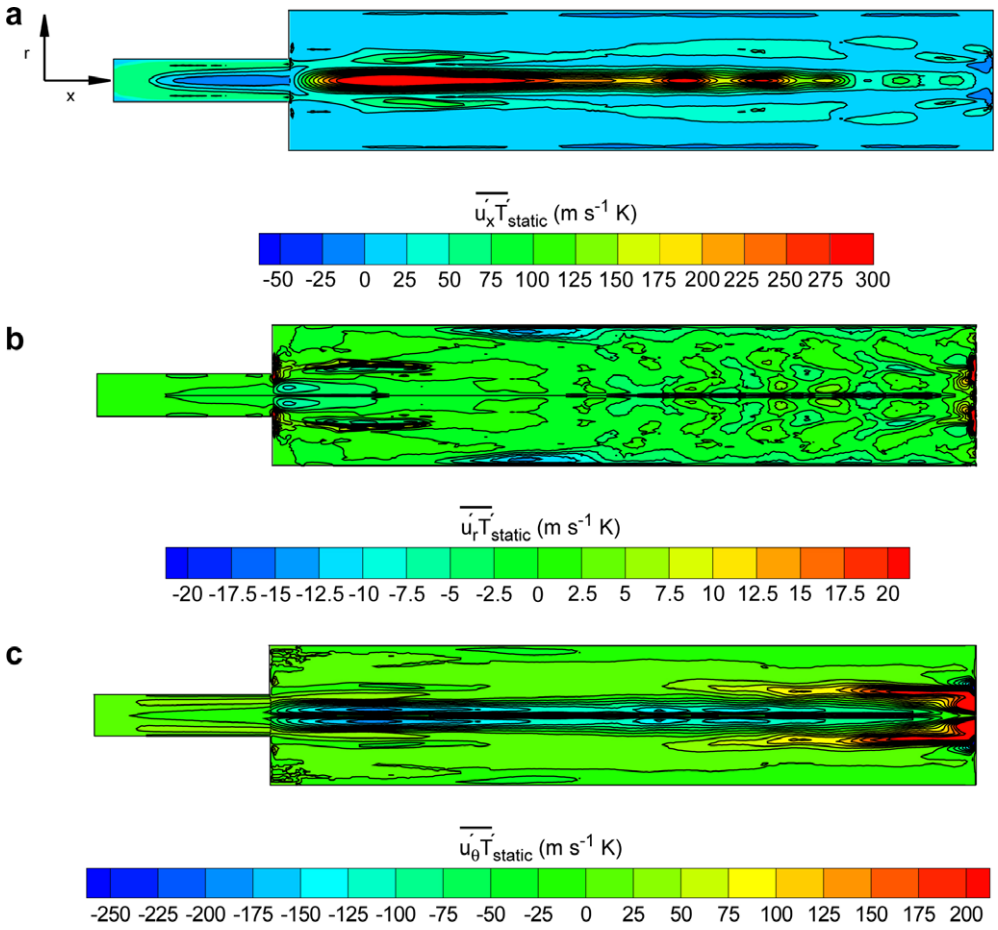

Fig. 12. Contours of (a) $\overline{u'_x T'_{static}}$ correlation (b) $\overline{u'_r T'_{static}}$ correlation and (c) $\overline{u'_\theta T'_{static}}$ correlation for the vortex tube in the r–x plane (case 1). The time average was performed between 0.4 and 0.8 s.

aration of 38.7 K was observed for a cold mass fraction of 0.39. Unlike the cold exit temperature separation the hot exit temperature separation $|\overline{T}_{total,hotexit} - \overline{T}_{total,in}|$ was found to increase with an increase in the cold mass fraction (Fig. 16b). A maximum hot gas temperature of 41.8 K was observed for a cold mass fraction of 0.69 (the largest value of the cold mass fraction used in simulation). The gas separation as function of cold mass fraction is presented in Fig. 17. Following Linderstrom-Lang the gas separation is the difference between the species content at the hot exit and cold exit ($\overline{Y}_{He,hotexit} - \overline{Y}_{He,coldexit}$). Similar to the temperature separation the time averaged helium mass fraction at the hot and cold ends was also spatially averaged to determine the

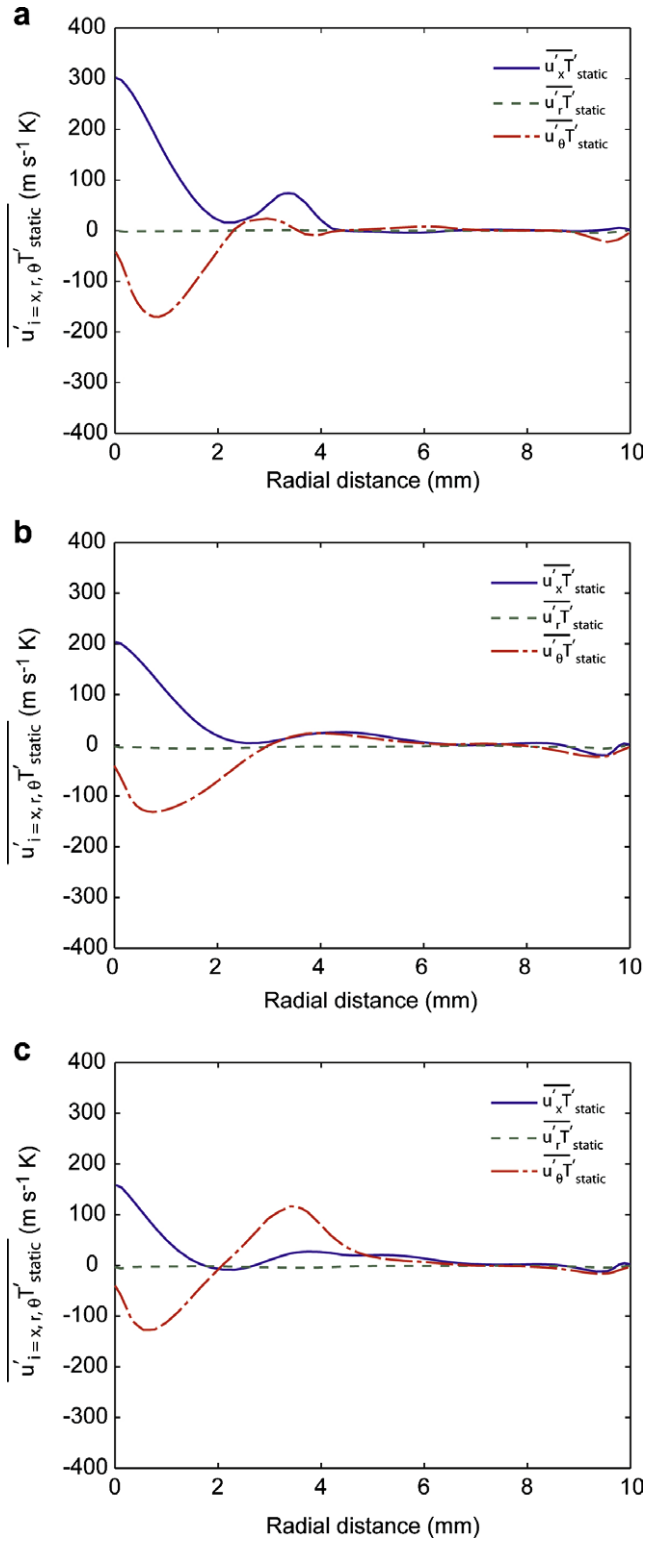

Fig. 13. Radial profiles of $\overline{u'_x T'_{static}}$, $\overline{u'_r T'_{static}}$ and $\overline{u'_\theta T'_{static}}$ correlation at (a) $x = 50$ mm (b) $x = 75$ mm and (c) $x = 100$ mm (case 1). Time averaging was performed between 0.4 and 0.8 s.

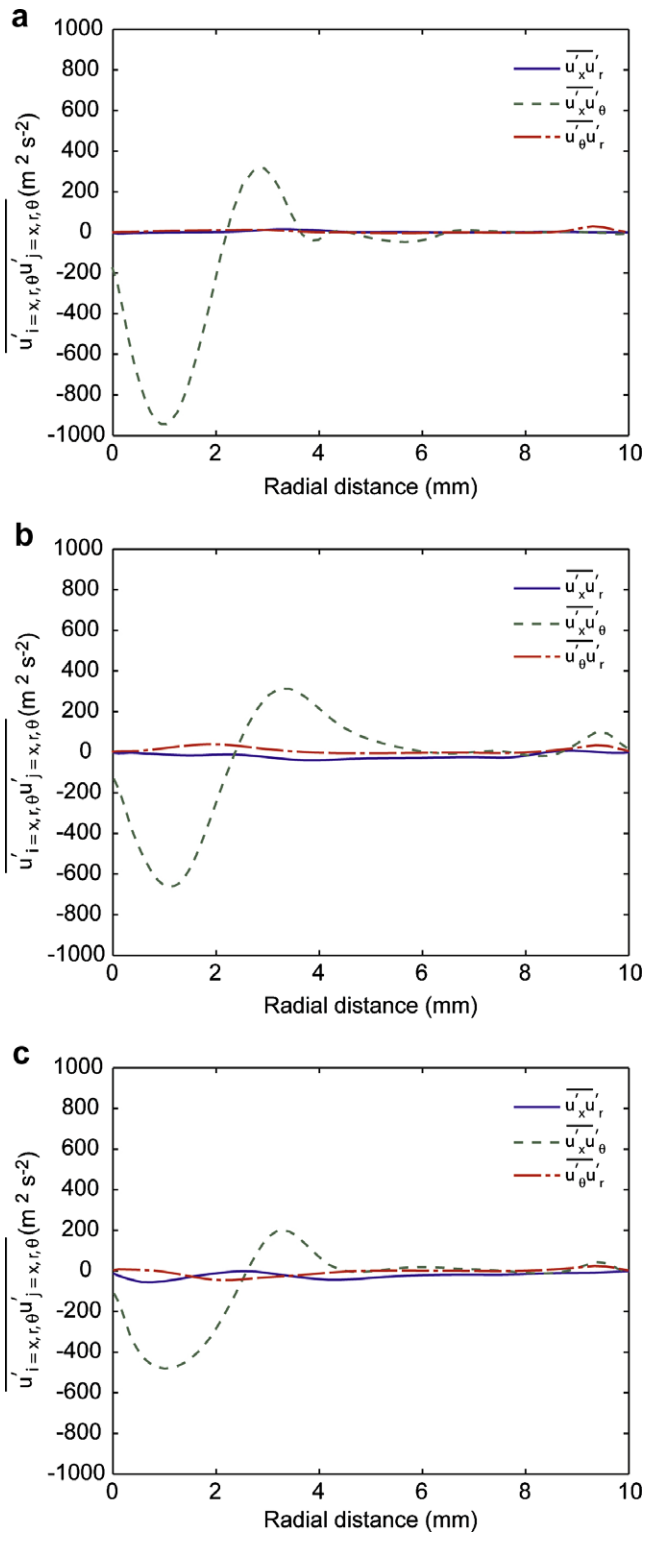

Fig. 14. Radial profiles of $\overline{u'_x u'_r}$, $\overline{u'_x u'_\theta}$ and $\overline{u'_\theta u'_r}$ correlation at (a) $x = 50$ mm (b) $x = 75$ mm and (c) $x = 100$ mm (case 1). Time averaging was performed between 0.4 and 0.8 s.

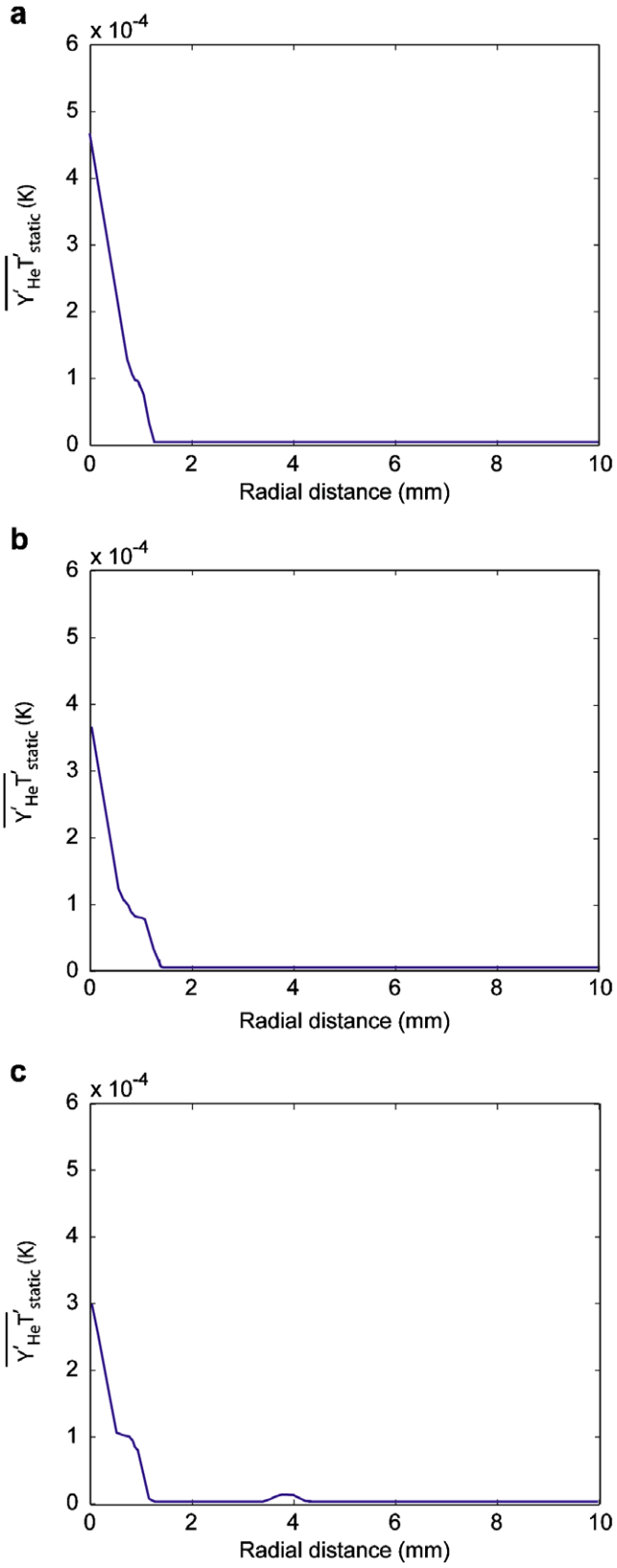

Fig. 15. Radial profiles of $\overline{Y'_{He}T'_{static}}$. Correlation at (a) $x = 50$ mm (b) $x = 75$ mm and (c) $x = 100$ mm (case 1). Time averaging was performed between 0.4 and 0.8 s.

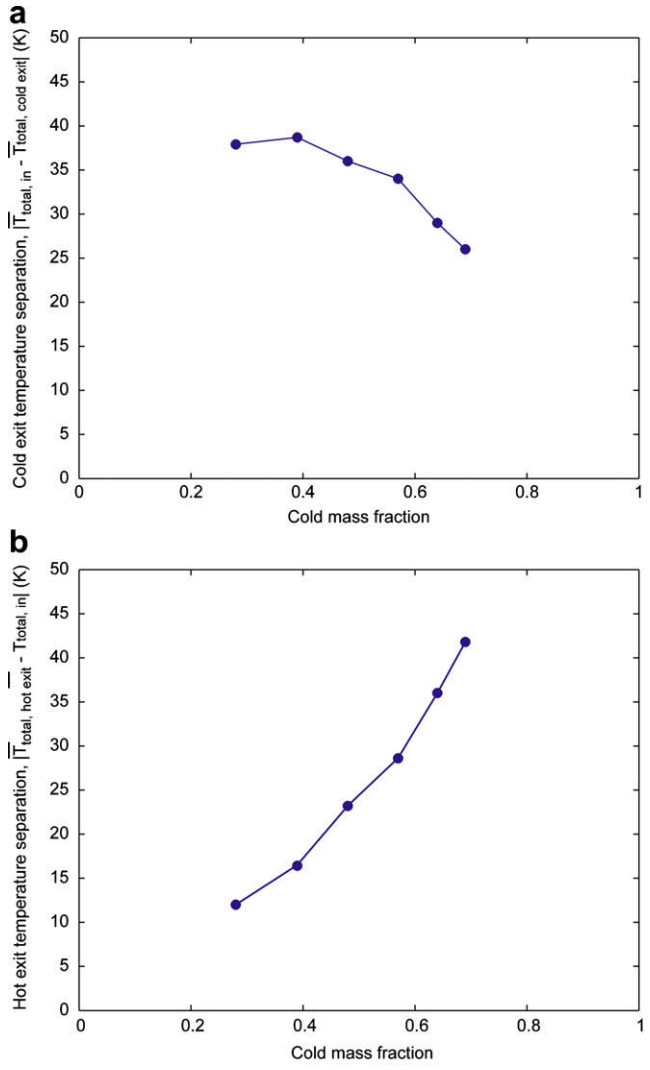

Fig. 16. (a) Cold exit temperature separation $|\overline{T}_{total,in} - \overline{T}_{total,coldexit}|$ and (b) hot exit temperature separation $|\overline{T}_{total,hotexit} - \overline{T}_{total,in}|$ as a function of cold mass fraction.

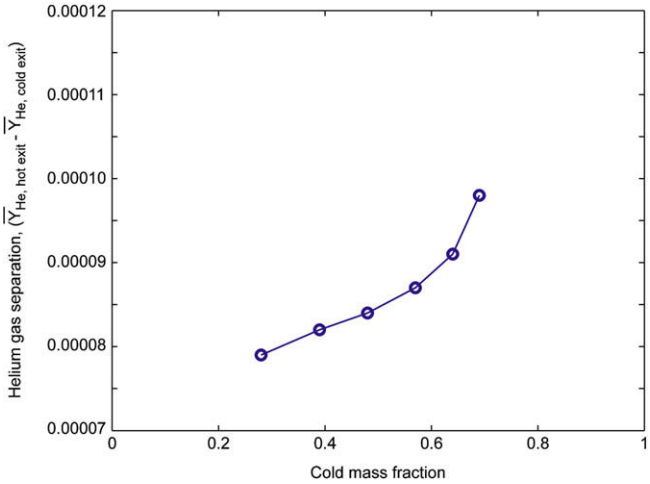

Fig. 17. Helium gas separation $(\overline{Y}_{He,hotexit} - \overline{Y}_{He,coldexit})$ as a function of cold mass fraction.

gas separation effect. The gas separation was noticed to increase with an increase in the cold mass fraction (Fig. 17). This is a consequence of the increased total temperature separation with increased cold mass fraction. The higher total temperature separation resulted in increased diffusion due to the Soret effect. The maximum gas separation was predicted to be $\sim 1.0 \times 10^{-4}$ for a cold mass fraction of 0.69.

5. Conclusions

Numerical simulations of gas species and temperature separation in a counter flow Ranque–Hilsch vortex tube for a nitrogen–helium gas mixture were conducted. LES technique was used to model the turbulence effects. The LES methodology is based on direct solution of the large scales and sub grid scale approximation for the dynamic viscosity. The simulations indicated the axial and azimuthal velocities to be the dominant components. In the inner core very negligible azimuthal velocity was predicted which is contrary to the general perception that in counter flow Ranque–Hilsch vortex tube, the entire core flow is a forced vortex. The small peripheral region was predicted to have free vortex like characteristics. The radial velocity which had the smallest magnitude was found to be directed towards the tube center through most of the tube volume and towards the tube near the wall. The instantaneous streamlines showed the presence of small vortices through out the vortex tube. However the small vortical structures were found to be more prominent in the inner core regime.

The time averaged profiles indicated a hot peripheral flow and a reversing cold inner core flow together with a small secondary circulation near the cold exit. The time averaged species mass fraction separation predicted in the simulation due to the Soret diffusion was found to have very small value. Correlations between the fluctuating components of velocity, temperature and species mass fraction ($u'_x, u'_r, u'_\theta, T'_{static}$ and Y'_{He}) were calculated to understand the separation mechanism. Large magnitudes of $\overline{u'_x T'_{static}}$ and $\overline{u_\theta T'_{static}}$ were present at the inner core, which suggested the presence of significant eddy heat flux in the axial and azimuthal direction. The $\overline{u'_x u'_r}, \overline{u'_x u'_\theta}$ and $\overline{u'_\theta u'_r}$ correlations revealed $\overline{u'_x u'_\theta}$ to be the dominant component. The large values of $\overline{u'_x u'_\theta}$ at the inner core suggested the presence of large Reynold's stresses due to the axial and azimuthal velocity components. Very weak correlation was found to be present for $\overline{Y'_{He} T'_{static}}$, which explains why such a small amount of gas separation occurred due to Soret diffusion.

The effects of cold mass fraction on the temperature and gas separation effect were studied. The cold mass fraction was varied by varying the hot exit pressure. Apart from the cold mass fraction range of 0.28–0.39 the cold exit temperature separation was found to decrease with an increase in the cold mass fraction. The maximum cold exit temperature separation of 38.7 K occurred for a cold mass fraction of 0.39. Unlike the cold exit temperature separation, the hot exit temperature separation was observed to increase with increasing cold mass fraction. The maximum hot exit temperature separation of 41.8 K was for a cold mass fraction of 0.69 (the largest value of the cold mass fraction used in simulation). Over the entire cold mass fraction range very small amount of gas separation was predicted. The gas separation was observed to be in the range of 0.8×10^{-4}–1.0×10^{-4} which is negligible for any practical consideration. Since the Soret diffusion was the governing mechanism for gas separation, the gas separation increased with increased cold mass fraction as a result of increased temperature separation effect.

References

[1] G.J. Ranque, Experiences sur la detente giratoire avec simultanes d'un echappement d'air chaud et d'un enchappement d'air froid, J. Phys. Radium 4 (7) (1933) 112–114.

[2] R. Hilsch, The use of the expansion of gases in a centrifugal field as cooling processes, Rev. Sci. Instrum. 18 (2) (1947) 108–113.

[3] H.H. Bruun, Experimental investigation of energy separation in vortex tubes, J. Mech. Eng. Sci. 11 (6) (1969) 567–582.

[4] B. Ahlborn, J. Camire, J. U Keller, Low-pressure vortex tubes, J. Phys. D: Appl. Phys. 29 (1996) 1469–1472.

[5] B. Ahlborn, J. U Keller, R. Staudt, G. Treitz, E. Rebhan, Limits of temperature separation in a vortex tube, J. Phys. D: Appl. Phys. 27 (1994) 480–488.

[6] C.M. Gao, K.J. Bosschaart, J.C.H. Zeegers, A.T.A. M De Waele, Experimental study on a simple Ranque–Hilsch vortex tube, Cryogenics 45 (2005) 173–183.

[7] W. Frohlingsdorf, H. Unger, Numerical investigations of the compressible flow and the energy separation in the Ranque–Hilsch vortex tube, Int. J. Heat Mass Transfer 42 (1999) 415–422.

[8] U. Behera, P.J. Paul, S. Kasthurirengan, R. Karunanithi, S.N. Ram, K. Dinesh, B. Jacob, CFD analysis and experimental investigations towards opitmizing the parameters of Ranque–Hilsch vortex tube, Int. J. Heat Mass Transfer 48 (2005) 1961–1973.

[9] N.F. Aljuwayhel, G.F. Nellis, S.A. Klein, Parametric and internal study of the vortex tube using a CFD model, Int. J. Refrigeration 28 (2005) 442–450.

[10] H.M. Skye, G.F. Nellis, S.A. Klein, Comparison of CFD analysis to empirical data in a commercial vortex tube, Int. J. Refrigeration 29 (2006) 71–80.

[11] C. Linderstrom-Lang, Gas separation in the Ranque–Hilsch vortex tube, Int. J. Heat Mass Transfer 7 (1964) 1195–1206.

[12] M. Kulkarni, C. Sardesai, Enrichment of methane concentration via separation of gases using vortex tubes, J. Energy Eng. 128 (1) (2002) 1–12.

[13] J. Harnett, E. Eckert, Experimental study of the velocity and temperature distribution in a high velocity vortex-type flow, Trans. ASME 79 (4) (1957) 751–758.

[14] B. Ahlborn, J. Gordon, The vortex tube as a classical thermodynamic refrigeration cycle, J. Appl. Phys. 88 (6) (2000) 3645–3653.

[15] K. Stephan, S. Lin, M. Durst, F. Huang, D. Seher, An investigation of energy separation in a vortex tube, Int. J. Heat Mass Transfer 26 (3) (1983) 341–348.

[16] M. Kurosaka, Acoustic streaming in swirling flows, J. Fluid Mech. 124 (1982) 139–172.

[17] A.F. Gutsol, The Ranque effect, Physics – Uspekhi 40 (6) (1997) 639–658.

[18] S. Eiamsa-Ard, P. Promvonge, Numerical investigation of the thermal separation in a Ranque–Hilsch vortex tube, Int. J. Heat Mass Transfer 50 (2007) 821–832.

[19] J. Anders, V. Magi, J. Abraham, A computational investigation of the interaction of pulses in two-pulse jets, Numer. Heat Transfer A: Appl. 54 (11) (2008) 999–1021.

[20] Y. Hu, L. Zhou, Y. Luo, Large-eddy simulation of the Sydney swirling non-premixed flame and validation of several subgrid-scale models, Numer. Heat Transfer B: Fundam. 53 (1) (2008) 39–58.

[21] A. Elhami, S. Kazemzadeh, F. Mashayek, Large-simulation of heavy particle transport in turbulent channel flow, Numer. Heat Transfer B: Fundam. 50 (4) (2006) 285–313.

[22] J. Lee, X. Xu, R. Pletcher, Large eddy simulation of the effects of inner wall rotation on heat transfer in annular turbulent flow, Numer. Heat Transfer A: Appl. 46 (4) (2004) 323–341.

[23] T. Farouk, B. Farouk, Large eddy simulations of the flow field and temperature separation in the Ranque–Hilsch vortex tube, Int. J. Heat Mass Transfer 50 (2007) 4724–4735.

[24] J. Smagorinsky, General circulation experiments with primitive equations, I. The basic experiment, Monthly Weather Rev. 91 (1963) 99–164.

[25] CFD-ACE Modules Manual V2004. Huntsville, AL: ESI US R&D, 2004.

[26] B.P. Leonard, Bounded higher-order upwind multidimensional finite-volume convection–diffusion algorithms, in: W.J. Minkowycz, E.M. Sparrow (Eds.), Adv. Numer. Heat Transfer, vol. 1, Taylor and Francis, New York, 1997, pp. 1–57.

[27] J. Beams, F. Haynes, The separation of isotopes by centrifuging, Phys. Rev. 50 (1936) 491–492.

[28] S. Whitley, Review of the gas centrifuge until 1962. Principles of separation physics, Rev. Mod. Phys. 56 (1) (1984) 41–66.

[29] L. Rayleigh, On the dynamics of revolving fluids, Proc. Royal Soc. Lond. Ser. A 93 (648) (1917) 148–154.

[30] M. Landahl, E. Mollo-Christensen, Turbulence and Random Processes in Fluid Mechanics, Cambridge University Press, Cambridge, 1992.

[31] H. Tennekes, J.L. Lumley, A First Course in Turbulence, MIT, Cambridge, MA, 1972.

[32] V. Kallinikov, A. Gutsol, A new efficient method of insulating high temperature and reacting systems and Ranque effect, Phys. Dokl. 42 (4) (1997) 179–181.

[33] A. Gutsol, J. Bakken, New vortex method of plasma insulation and explanation of the Ranque effect, J. Phys. D: Appl. Phys. 31 (6) (1998) 704–711.